Science and Technology Indonesia
e-ISSN:2580-4391 p-ISSN:2580-4405
Vol. 11, No. 3, July 2026

Research Paper

LEDs with Organized InGaN Nanopylons Generating within Green, Yellow, as well as Blue Region

Phan Xuan Le[1*], Nguyen Huy Khiem[1]

[1]Faculty of Electrical Engineering Technology, Industrial University of Ho Chi Minh City, Ho Chi Minh City, 70000, Vietnam
*Corresponding author: phanxuanle@iuh.edu.vn

Abstract
The creation of structured settings for InGaN/GaN (I/G) nano-pylon diodes emit illumination (LED) within the green, yellow, as well as blue (GYB) spectrum regions using molecular beam epitaxy has been described. Compared with InGaN (planar) sheets of identical structure and thickness, the gadget's working area, including one nano-pylon InGaN part for titularly identical element as well as lengthiness between 250 and 500 nm, would be unaffected by prolonged problems. Electroluminescent hue ranges indicate a minor blue change with rising power (nearly non-existent in the yellow gadget) and line wideness that are marginally wider than those of modern InGaN quantum wells. InGaN was also utilized in a phosphor-transmuted white LED (WLED) to enhance its optical attributes such as scattering, lumen, and color rendition. It was found that InGaN has its own advantages and limitations. It was found that adjusting the InGaN discharge to 460 nm would benefit the lumen and color rendition of the WLED under a particle size of 9 μm, while a 450-nm discharge would promote scattering, both of which better match the human sight.

Keywords
WLED, Luminous Flux, Color Quality, InGaN, Quantum Well

Received: 13 November 2025, Accepted: 15 March 2026
https://doi.org/10.26554/sti.2026.11.3.827-843

1. INTRODUCTION

Because of their ability for producing luminescence in the UV to IR region, InGaN materials are a great option for LED covering the entire observable spectrum and further. LEDs frequently depend on multi-quantum well (MQW) architectures that achieve the highest exterior quantum effectiveness (EQP) at a modest current injection, usually less than 10 A cm^{-2}. Especially under pulsed current settings, where self-heating impacts are prevented, the so-called effectiveness 'droop' is evident at larger injection currents. Many theories, including carrier overbrim and Auger re-mixture, were proposed for clarifying the sink phenomenon (Qin et al., 2025; Grzanka et al., 2025; Bercha et al., 2025). Auger re-mixture correlates with the tertiary energy for the conveyor denseness (n^3), implying that raising the activating area volume of the gadget would significantly lessen its influence. Several researchers have suggested and followed this technique, which employs a double-hetero-layout InGaN activating sheet that is denser than a normal QW yet remains in 10 - 20 nm region (Aktas et al., 2024; Lee et al., 2024). According to the circumstances, the EQP has increased, with the maximum value migrating upward to greater currents. Nevertheless, the strategy would be useful just in case the thicker InGaN sheets had adequate properties, i.e. no out of joints, which can be obtained partially by employing standalone GaN layouts (Jafar et al., 2023). Actually, using these low-defect materials for growing LEDs with typical InGaN MQW activating areas has been proven to move the highest EQP location towards greater currents (Yang et al., 2023). However, because ineffective electron internment in the InGaN activating area is one of the causes of current overbrim, a thicker area might additionally assist in minimizing this issue, although different methods, including the application of electron-preventing sheets (Wang et al., 2023; Barettin et al., 2023), are becoming increasingly common.

LEDs constructed from settings for auto-constructed nanopylons (NPs) featuring integrated InGaN quantum discs (Q-Disks) or motes (QMs) were proposed to be a substitute for planar gadgets lately (Gu et al., 2023; Hsieh et al., 2023). The benefits from NP-derived LED apparatuses would be two-fold: i) increased illumination exploitation effectiveness (ignoring a requirement for expensive technological procedures) by utilizing the directing capabilities inherent in these 'cylindrical' nanolayouts (Huang et al., 2023; An et al., 2023; Sun et al., 2023) and ii) activating sheets having extremely elevated crystalline standard and low tension. Nevertheless, self-formed NCs have significant limitations, including inherent poly-chromaticity and high geometrical and electrical spread, which make it difficult to produce and reduce effectiveness (Miao et al., 2023; Qiu et al., 2025). To deal with such problems, molecular beam epitaxy (MBE) particular region increase (SAG) of III-nitride NCs has been developed in the past few years, resulting in strongly uniform and manageable settings for I/G nano-pylon hetero-layouts containing either built InGaN QDisks (Han et al., 2026) or extensive InGaN parts (Xu et al., 2025; Duan et al., 2025). LED apparatuses constructed from arranged sets of NCs producing in the green (Cong and Anh, 2025; Hadi et al., 2025) and red ranges (Rianjanu et al., 2025), and also an InGaN portion with an 80-nm breadth producing within the close-infrared region (Zhou et al., 2025), were just lately shown.

InGaN semiconductor components are integral to the essential optical discharger within phosphor-converted WLED devices, providing several key functions, including efficient blue photon generation, wavelength-tunable illumination through In composition adjustment, and a broad spectral range via multi-wavelength emission. These attributes assist InGaN in overcoming inherent limitations of conventional illumination and enable the adoption of advanced phosphor configurations. WLED devices can achieve high luminous efficacy by leveraging the ability of InGaN to produce intense blue photon granules, which excite phosphor down-converters, thereby yielding high color rendering indices across adjustable correlated color temperature levels (Oh et al., 2025). The operation of phosphor-transmuted WLED devices depends extensively on InGaN as a primary illumination component. The semiconductive component generates blue or near-ultraviolet photonic granules through radioactive recombination within quantum well or quantum dot functional layers, which are subsequently absorbed by phosphor materials, including $YAG:Ce^{3+}$ and $K_2SiF_6:Mn^{4+}$. This configuration proves to be widespread, as InGaN exhibits a tunable bandgap ranging from infrared to ultraviolet, enabling precise control of the emission wavelength through the In composition.

This paper describes the development, manufacturing, and feature of GYB LED apparatuses (p-i-n architectures) utilizing organized NCs having substantially longer InGaN activating areas. Regarding the use of LEDs, the findings indicate to this particular shape as an appropriate substitute for the usage of integrated InGaN QDisks in addition to traditional planar designs utilizing QWs. Furthermore, the ability to grow thick InGaN parts built on p-i-n organized NCs with no traces of raised imperfections, as stated in the present study, compared to the standard outcomes for planar buildings, renders this type of configuration particularly attractive for solar cells (Yan et al., 2025; Zheng et al., 2025). Unlike previous studies which solely focus on assessing InGaN nano-pylon in LEDs, the research herein extends its focus to integrating InGaN in WLED apparatuses, and seek potential ways to enhance their optical attributes and broaden possible application to various settings such home, workplace, street, and industrial lighting (Anh et al., 2025a).

2. EXPERIMENTAL SECTION

2.1 Synthesizing InGaN Samples

SAG was used for growing every specimen of commercial GaN(0001)/sapphire designs within one RIBER Compact 21 PA-MBE setting. Growth rate units (nm/min) were used for calibrating the impacting molecular fluxes of (0001) GaN and (0001) InN (Cakmakci et al., 2021). Before development, the templates were coated using one narrow Ti overlay containing one tight hexagon latticework featuring colloidal lithography nanocavities. This approach is described in detail elsewhere (Hou et al., 2021). The duration (P, spacing among cores of nearest holes) of the nanohole lattice was 280 nm, while the diameter was roughly 150 nm. The mask configuration revealed the NCs denseness to be $\sim 1.15/P^2 \sim 1.5E9$ cm^{-2}. The starting fill rate was 0.26, which refers to the proportion of the NCs footprint to the wafer region. Nevertheless, the NC size rose throughout the formation of the InGaN/GaN:Mg nanocolumnar parts owing to the influence of In and Mg on the radial growing speed (Xiong et al., 2021; Wang et al., 2021), shown by Figures 1(a), 1(b) and 1(c), leading the filling rate to rise to 0.72.

Dual sampling units, S1 and S2, of nano-pylons featuring loaded GaN:Mg/InGaN/GaN:Si partitions (p-i-n formations) were developed with a triple-stage procedure. Firstly, the development of GaN:Si nano-pylons was conducted within two hours and a half under 860 °C accompanied by a Si cellule heat level reaching 950 °C. Secondly, the development for one InGaN partition was conducted within one hour under 650 °C with S1 and within half an hour with S2. Thirdly, the development for GaN:Mg within half an hour was conducted under 600 °C via one Mg cellule heat level reaching 365 °C. While identical developing states were employed for the InGaN development within said samples, it is possible to construct the LED apparatuses discharging between blue and yellow. Said mechanism resulted from a heat incline reaching roughly 20 °C across the sheet throughout the MBE development with the greatest heat level upon the sheet's rim, causing a variance in In integration between the sheet's central point (bigger In percentage) and the rim (smaller In percentage).

2.2 Constructing Apparatuses

Several separate apparatuses were made via said sampling units, including apparatus 1 (A1) discharging within the blue zone generated by sample S1, apparatus 2 (A2) discharging within the green zone, as well as apparatus 3 (A3) discharging within the yellow zone, with the latter two zones generated by sample S2. Said apparatuses feature a round form, determined via mesa engraving, with diametric magnitude reaching 100 μm. The n-category proximity featured a standard Ti/Al/Ti/Au electrode positioned via electronic ray vaporization upon GaN foundation. Above the nano-pylons, one Ni/Au p-category electrode was positioned via thermic vaporization, utilizing Au for guaranteeing appropriate current extension. Thermic vaporization was conducted via one incidental angle reaching roughly 30° as well as sample alternation. The tiny range

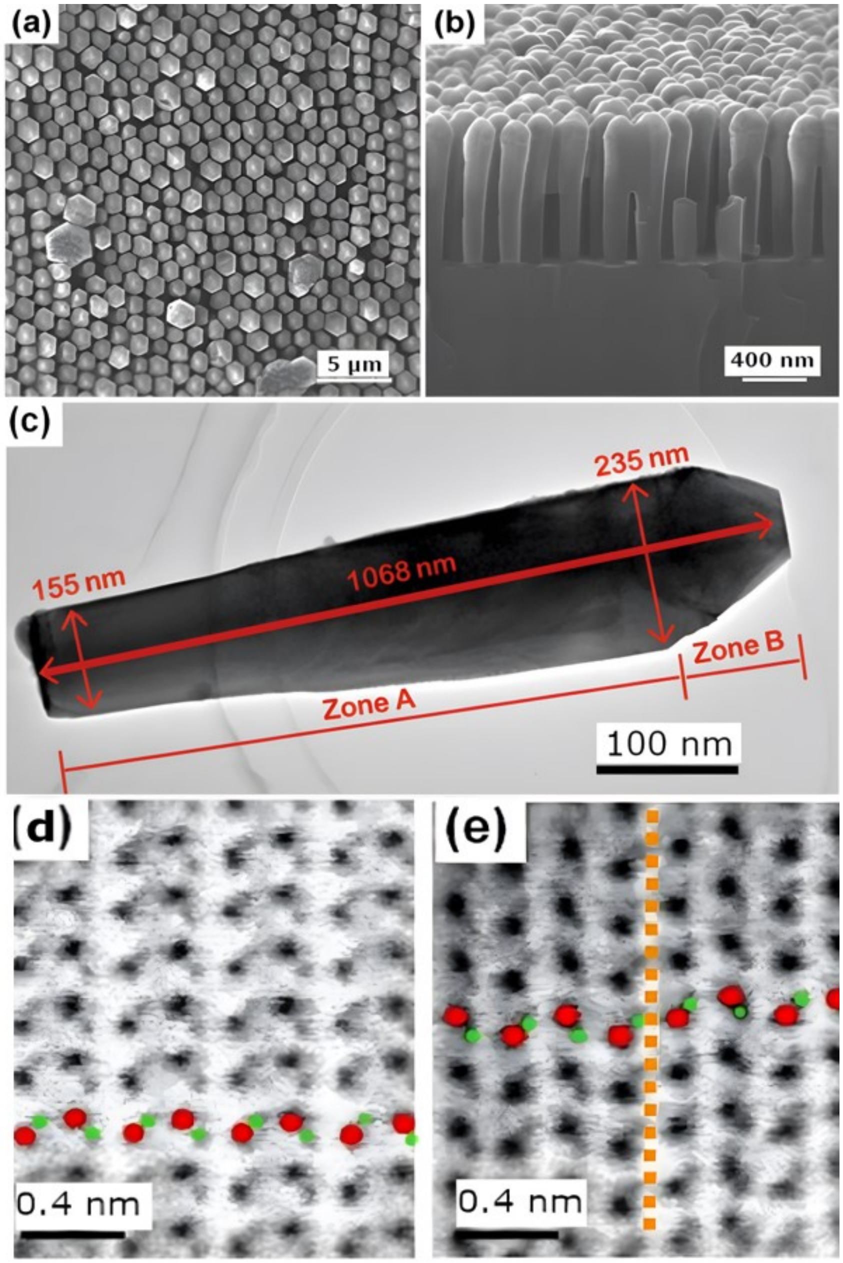

Figure 1. Characterization Data of Sample S1: (a) SEM Visual of InGaN Nano-Pylon (Top View), (b) SEM Visual of InGaN Nano-Pylon (Cross-Sectional View), (c) TEM Visual of Nano-Pylon in Sample S1, (d) and (e) Respectively Exhibit Granularly-Solved STEM Visuals for GaN:Si/InGaN (Zone A) and GaN:Mg (Zone B)

among nano-pylons with maximal pervading factor reaching 0.72 assists the metallizing process for the highest proximity via straightforward vaporization, with no pervading substance among nano-pylons. The tempering states regarding ohmic proximity would be five minutes under 450° subject to H_2:N_2 aerosphere. The illumination was gathered via a sapphire substrate, causing a potent illumination intenseness abatement to 1 or 2% of its initial outcome because of the interfacial planes between GaN and sapphire as well as sapphire and air.

2.3 Characterization

The nano-formations as well as apparatuses were examined via scanning electronic microscopic (SEM) assessment, transference electronic microscopic (TEM) assessment, as well as scanning transference electronic microscopic (STEM) assessment. High-resolution TEM, SEM, STEM as well as granular resolution assessment were conducted upon one JEOL JEM ARM200cF electronic microscopic apparatus (chill discharge) with STEM mode functioning under 200 kilovolts accompanied by one globular divergence rectifier. Hard quasi-angle

Table 1. Result Comparison of Scattering Coefficients Influenced by Particle Sizes of Scattering Materials

Scattering Materials	Scattering Coefficients (mm^{-1})	Reduced Scattering Coefficients (mm^{-1})	References
InGaN	0.79	0.00055237	This work
SiO_2	9.16	0.78	(Le et al., 2024)
KBr	42.5	13.5	(Anh et al., 2025b)

units from 11 to 22 mrad were utilized to obtain circular glowing zone (CGZ) visuals utilizing an obtaining duration reaching 38 s each frame. Additionally, the nano-formations were examined via I-V assessments as well as room temperature pulsated electroluminescence (EL) featuring 1% duty rotation as well as 1 μs pulsation. EL assessment was conducted using a QEPro OceanOptics spectrometer operating in emission (luminescence) mode accompanied by an integrating sphere.

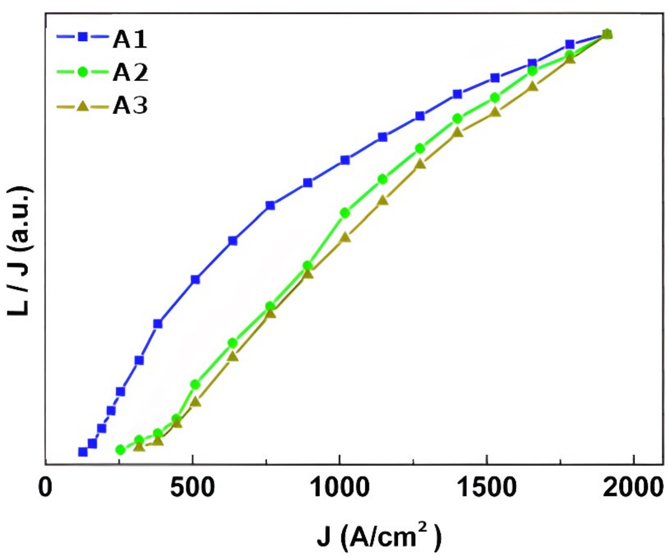

Figure 2. L/J against J Reliance for Apparatuses A1, A2, and A3

3. RESULT AND DISCUSSIONS

3.1 Optical Assessment of LED Based on InGaN Nano-Pylons

The small magnified visual for a typical nano-pylon casted unto the (010) surface is exhibited via Figure 1(c). NPs feature a wurtzite-kind crystalline layout straightforwardly perceived within the granularly-solved STEM visual exhibited via Figure 1(d), displaying the arrangement for the Ga as well as N granular pylons. There is a lack of formational flaws within the GaN:Si/InGaN parts shown via zone A within Figure 1(c), but upon the peak of nano-pylon shown via zone B within Figure 1(c), the creation of twin boundaries at the top of the NCs creates one sole-film of a blende-kind configuration, shown by dashed line in Figure 1(e). The minimal-heat development of the top p-kind GaN portion is probably to blame for the formation of these extensive structural flaws. Due to the absence of successive twins, the construction of an expanded blende-kind configuration above the NCs can be excluded. While the equipment's current-voltage (I-V) properties demonstrate a non-zero leakage current, a rectifying behavior that produces an acceptable turn-on voltage is discovered. Because no filler substance was employed to separate/ inactivate the NCs, the upper ohmic connection might partly short-circuit the p- as well as n-places, causing the leak seen. Surprisingly, apparent relationship among emitting wavelength as well as triggering voltage did not manifest. The explanation to clarify said mechanism remains unknown, prompting investigation. One hypothesis is that the In dispensation within the NCs, for example, within apparatus A1, producing within the blue spectrum, there are patches of increased In-substance that suppress generation at reduced insertion currents, which is going to be explained subsequently. Considering that extracting effectiveness is not affected by stimulation, the EQP corresponds to the proportion of integrated EL strength (L) to current density (J). Given the setup constraints, no absolute EQP values may be supplied. Figure 2 depicts the L/J proportion correlating with current denseness for three gadgets with barely any proof for effectiveness sink. For conventional flat LED apparatuses, EQP is greatest at current denseness of roughly 10 A cm^{-2} or less, with effectiveness drooping at larger insertion denseness. Particularly in select techniques, most of which use low-defective underneath materials, can the highest EQP level be shifted to greater currents (Le et al., 2026). Elevated current denseness would be achieved while avoiding effectiveness sink for gadgets that utilize built-in NCs, yielding denseness possibly reaching 2200 A cm^{-2}.

Based on the ABC designs it is possible to describe EQP using the following factors into consideration: The SRH factor, denoted A, is connected to non-radiative recombine at crystal flaws; the radiative factor, denoted B; and the non-radiative Auger factor, denoted C. The greatest effectiveness is attained as the conveyor denseness (n) is (A/C)0.5, according to this calculation. The gadgets reported here have a significantly higher activating area than normal QWs-based gadgets, resulting in a lower carrier denseness for a given insertion current denseness. As a result, the EQP will reach its maximum at larger current denseness than in conventional QW-based gadgets. Figure 2 suggests that the EL tests were performed at a low enough carrier denseness that the EQP maximum was not attained. In contrast, considering the lack of prolonged flaws, the reality that the EQP maximum is not attained with elevated injection might suggest an elevated fault associated non-radiative re-mixture, which would be unexpected in this situation, as

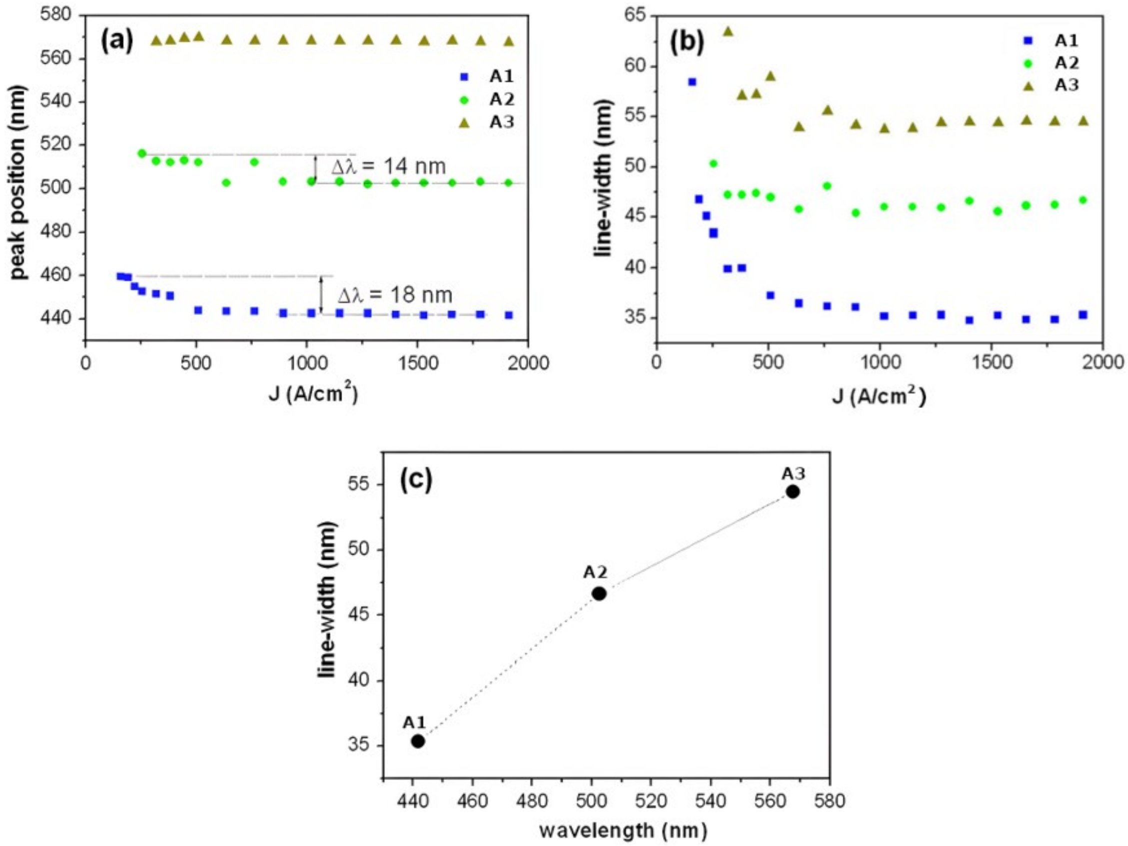

Figure 3. EL Bandwidth Data of Three Apparatuses: (a) EL Apex Wavelength Reliance Upon Current Denseness Signifying Apex Shifts of Apparatuses A1 and A2, (b) EL Spectrum Bandwidth Development Alongside Current Denseness of Apparatuses A1, A2, and A3, (c) EL Spectrum Bandwidths of the Three Apparatuses Under the Maximal Administered Current of 150 Milliamperes

seen via Figure 1 (Thong et al., 2022). Nevertheless, given the gradual increase of L/I data as you increase injection and the fact that the NCs are not treated, intense non-radiative outermost covering re-mixture at the InGaN sidewalls may occur, resulting in a decrease of injection effectiveness and consequently inner quantum effectiveness, as demonstrated in built-in nanocolumnar LEDs. Regarding this, there is no solid evidence of the lack of the droop influence. The development for the EL apex wavelength alongside current denseness regarding the triple apparatuses is displayed in Figure 3(a), while the matching alterations apply to apparatuses A1 as well as A2. Apparatus A3 does not exhibit wavelength alteration, whilst apparatus A2 exhibits one blue-shift reaching 14 nm inside the current denseness span from 254 to 891 A cm^{-2}, preceding a nearly constant outcome reaching the maximal administered current. An identical mechanism applies to apparatus A1, exhibiting the biggest blue-shift at roughly 18 nm from 159 to 509 A cm^{-2} out of every apparatus.

Figure 3(b) exhibits a behavior of bandwidth abatement under current administration within every apparatus, with more noticeable activity in the case of A1, till a stable outcome is obtained over 1000 A cm^{-2}, surpassing A3, as well as a nearly insignificant influence in the case of A2. Under the biggest administration current of 150 milliamperes, the determined EL bandwidths would be respectively 35, 45, as well as 55 nm in the case of blue (441 nm), green (502 nm), as well as yellow (568 nm) apparatuses, as shown by Figure 3(c). An identical behavior was seen regarding level LED apparatuses associated with quantum well (Le et al., 2025; Enya et al., 2009), specifically 20, 35, as well as 50 nm in the case of blue, green as well as orange LED apparatuses, was clarified via boosting alloy disarray to gain greater In presence. The greater bandwidths outcomes determined within A1, A2, and A3 LED apparatuses may result from several mechanisms. Firstly, the minor variances for nano-pylon diametric magnitudes caused by an imperfectly conventional colloid veil and subsequently In presence and hence extending the EL spectrum. The influences upon nano-pylon diametric magnitude are shown via Figure 1(a). Secondly, the In percentage allocation inside the InGaN partition upon every nano-pylon is caused by latticework towing as well as InGaN thermic degradation (Kong et al., 2012; Albert et al., 2013). Notably, the EL spectrum bandwidths for A1, A2, as well as A3 apparatuses would be thinner compared to the counterparts in the case of LED apparatuses utilizing

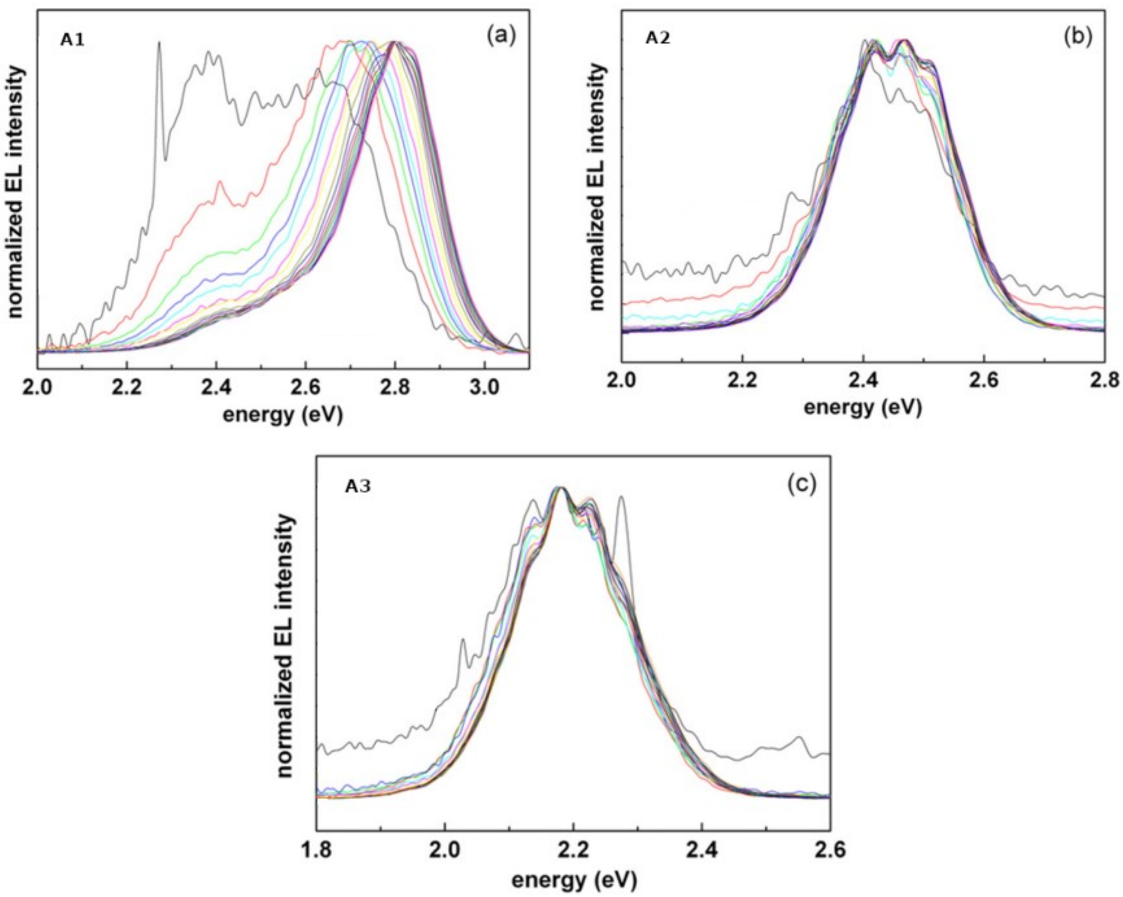

Figure 4. EL Spectra of the Three Apparatuses: (a) EL Spectra of Apparatus A1, Between Small Administered Current (10 Milliamperes) and Huge Administered Current (150 Milliamperes) (Under Small Administration, Discharge Would Be Generated via Dual Apexes with Identical Intenseness, Whilst Under Huge Administration, the Small Power Apex Would Be Abated), (b) and (c) Respectively Exhibit the EL Spectra of Apparatuses A2 and A3

structured nano-pylons featuring InGaN QDisk functioning zones (Kishino et al., 2013).

The standard blue-shift as well as bandwidth shrinkage seen for InGaN QW units as well as QDisks under surging exciting process can be clarified via assessing the intrinsic electrical field (Cong et al., 2025). An identical behavior would apply to the apparatuses assessed within the study herein, as shown by Figures 3(a) as well as 3(b). However, for said circumstance, the likeliest clarification depends upon the existence of local statuses inside the InGaN partitions. For the study herein, there is a possibility that disparate allocations as well as deepness for the said statuses might manifest within the triple apparatuses. For blue LED apparatus A1, a small-denseness allocation for local statuses might manifest near the conducting band (CB) nadir. In contrast, an allocation for local statuses featuring greater denseness as well as deepness, but far broader power extension for combining with the CB, might manifest within apparatuses A2 as well as A3 because of greater In presence. Additionally, it is necessary to consider that the leftover n-category conveyor denseness surges under surging In percentage, causing disparate positions for the Fermi state regarding the CB rim within the triple apparatuses. With the disparities of localization as well as Fermi state location, the power blue-shift as well as abatement in Full Width under Half Maxima (FWHM) under surging administration current may be partly clarified.

For apparatus A1, the Fermi state location is presumably minimally atop the local statuses. Under low administration current, discharge generated by local statuses presumably becomes prevalent (small power apex). Under surging administration current, the Fermi state will move towards the CB and as such, the EL discharge become influenced via the CB statuses (huge power apex). Because of the far bigger state denseness (SD) within the CB, an abatement for the bandwidth under surging administration current will become visible. Said mechanism would be supported via the readings of EL spectrum shown by Figure 4(a), in which dual solved EL apexes featuring identical intenseness can be seen under small current administration with an apex under greater power (discharge generated by the CB) and another apex under smaller power (discharge generated by local statuses). Upon boosting the current ad-

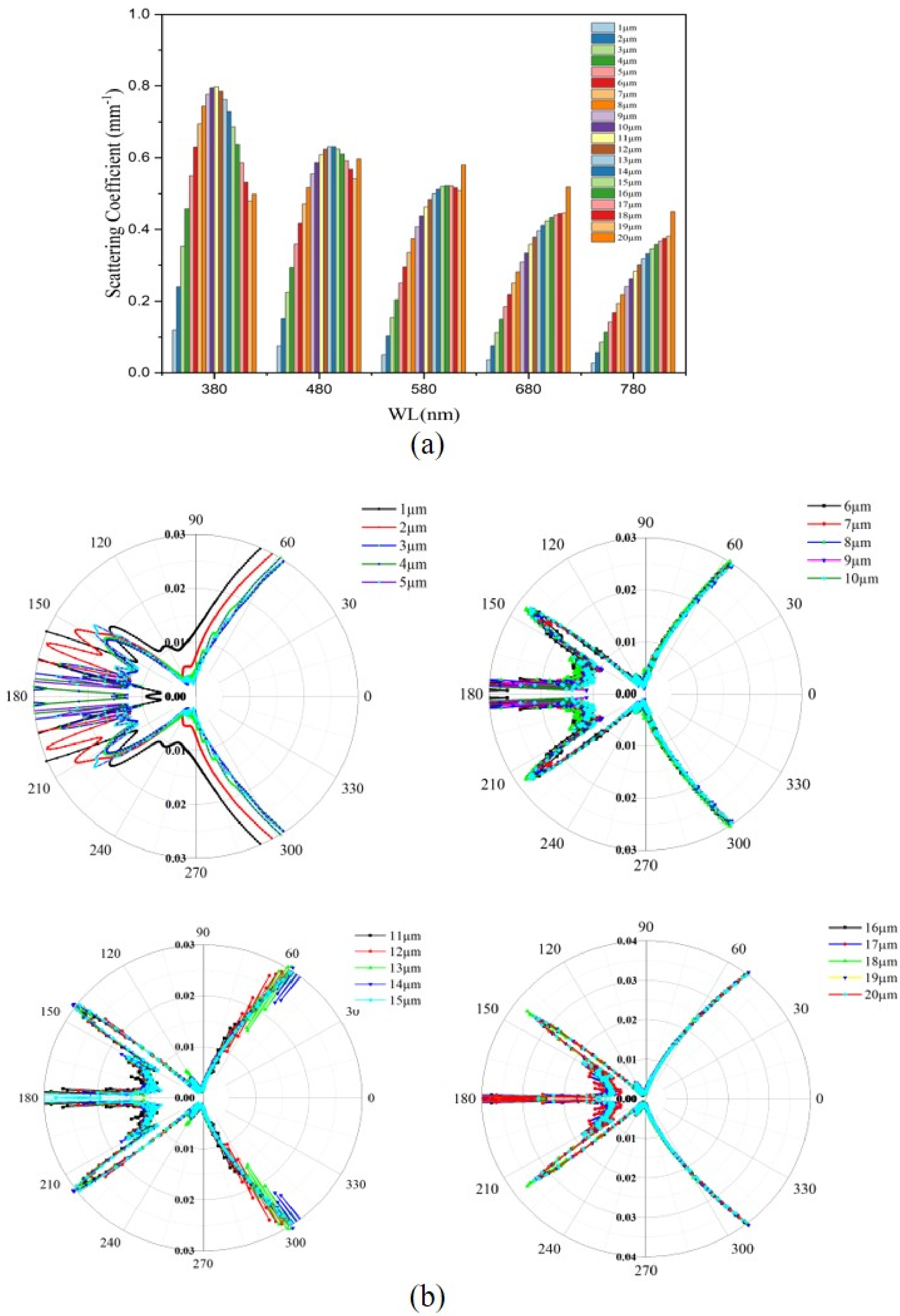

Figure 5. Scattering Factors of InGaN Particles: (a) Scattering Coefficient under Wavelengths, (b) Scattering Coefficient under Angles

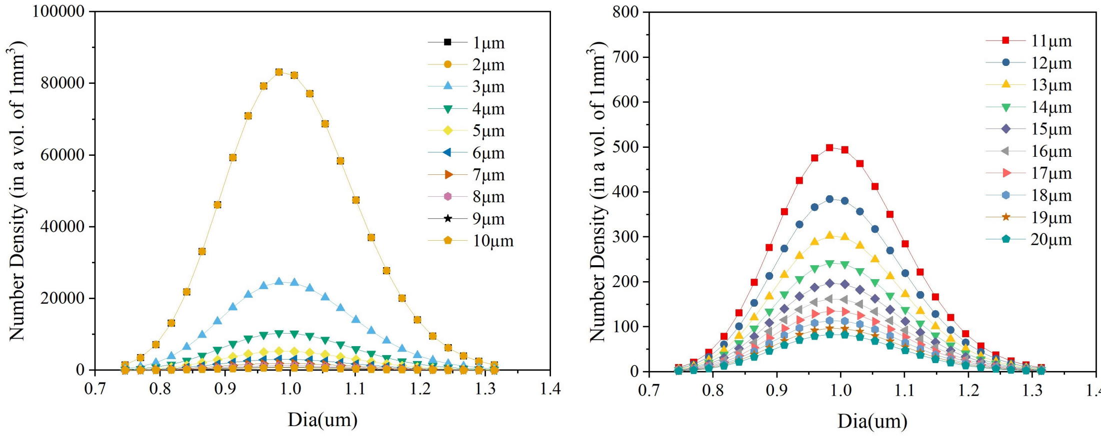

Figure 6. YAG:Ce Content Under Particle Sizes of InGaN

Table 2. Comparative Tables of this Research Results with Reported Research

Scattering Materials	YAG:Ce^{3+} (%)	CCT (K)	D-CCT (K)	CRI	CQS	Lumen (lm)	References
InGaN	27.4	3000	46.74	56.26	42.41	73.44	This work
SiO_2	27.4	3000	30	56.3	42.5	73.7	(Le et al., 2024)
KBr	27.4	3000	35.4	56.2	42.4	73.7	(Anh et al., 2025b)

ministration, the greater power apex proves to be prevalent (far bigger CB SD) accompanied by the concurrent shrinkage for the discharge apex. Notably, substantial alteration of the Fermi state presumably manifests as the CB is attained. Said presumption would be realistic under the consideration of proficient reconsolidation for conveyors along with the significant weights (level band) for nitride substances.

For the green A2 as well as yellow A3 apparatuses, with their EL spectra shown by Figures 4(b) as well as 4(c), the EL apex breadth under small administration current presumably cast back the power extended for every local status (combining with the CB), contributing to the discharge because of the Fermi state location atop them, which results from the greater In presence. A surge in the administration current will begin pervading the local statuses that feature a far greater SD compared with apparatus A1, along with the CB statuses when every local status, once again resulting in a blue-shift along with an abatement for the bandwidth regarding the blue apparatus, though far less harsh because of the greater SD for the local statuses within apparatuses A2 as well as A3.

Regardless, it is necessary to consider that the blue-shift, along with the bandwidth abatement, would be associated with disparate pervading statuses for the local statuses within the InGaN mass. As the central point for said mass presumably possess a greater In presence, surpassing the rims (Tourbot et al., 2011), under a small administration current, there is a reason to presume that the conveyors have a high chance of pervading the local statuses reaching the central point of the InGaN mass, whilst upon the rims for the focal region, the pervasion would become smaller. Because of such an ununiform saturating extent, the discharge will become relatively wide. Under surging administration current, the focal (saturated) reconsolidation zone has a high chance of extending across the whole InGaN mass. Ultimately, the saturation for local states expands across the whole InGaN mass and hence abating the bandwidth. Said influence will become more noticeable in the case of apparatuses A2 as well as A3 because of the greater span for the InGaN partition.

3.2 Influence of InGaN Particles on Scattering Coefficient in Phosphor-Transmuted WLED

In addition to nano-pylon LED, InGaN was also utilized to improve the optical attributes of WLED apparatuses when integrated into their phosphor components. The link among the improvements of InGaN component in LEDs and phosphor-derived WLEDs involves multiple optical as well as physical attributes. Although LEDs utilizing nano-pylons discharge chromatic illumination in a straightforward way, phosphor-transmuted WLED apparatuses utilize blue or UV LED apparatuses for exciting phosphors, with the enhancements for the key illumination means straightforwardly influencing the proficiency as well as chroma performance for the transmuted white illumination (Zhao et al., 2019). InGaN semiconductive components is a part of the essential optical discharger within phosphor-transmuted WLED apparatuses with multiple key augmenting functions, including strong-proficiency blue photonic inducement, wavelength-adjustable illumination inducement through In constitution regulation, as well as wide spectrum span via discharge with multiple wavelengths (Trang and Anh, 2025). Said attributes help InGaN bypass innate restrictions for conventional illumination and facilitate newer phosphor settings. WLED apparatuses can attain high lumen proficiencies via benefitting from the capability of InGaN of generating strong-proficiency bleu photonic granules which excite phosphor down-transmuters, resulting in high chroma rendition indices throughout adjustable correlated chroma temperature levels (Oh et al., 2025). The setting of phosphor-transmuted WLED apparatuses relies heavily upon InGaN in the form of a key illumination means. The semiconductive component induces blue or n-UV photonic granules via radioactive recombination within quantum well or quantum mote functioning sheets, subsequently absorbed via phosphor substances, including YAG:Ce^{3+}, K_2SiF_6:Mn^{4+}. Said setting proves to be prevalent since InGaN displays a shifting bandgap, spanning between infrared and UV, facilitating accurate regulation of discharge wavelength via In constitution. Blue InGaN LED apparatuses usually function with between 18 and 25% In presence within the functioning sheet to generate photonic granules under 450 nm (Baheti et al., 2023).

Figure 5 demonstrates the link between particle sizes of InGaN and light distribution. For phosphor-transmuted LED apparatuses, the InGaN/GaN chip usually discharges a thin blue spectrum peaking under roughly between 450 and 470 nm (Anh et al., 2025b) alongside a cosine Lambertian angle data. Said blue illumination would be responsible for pumping the YAG:Ce^{3+} sample. Since InGaN LED apparatuses discharge non-polar illumination posterior to a Lambertian allocation, the preliminary photonic granules go into the YAG:Ce^{3+} sheet across a wide angular span. The apex wavelength as well as spectrum breadth for the InGaN discharge will decide the way it influences the wavelength-reliant dispersion as well as absorptivity of the phosphor. YAG:Ce^{3+} shows potent absorptivity from roughly 450 to 470 nm and discharges wide yellow illumination at roughly 550 nm. Based on the Mie dispersion hypothesis, the scattering coefficient of YAG granules would be determined via Equation (1) (Trang et al., 2019):

$$\mu_s(\lambda) = \rho \cdot \sigma_{scat}(\lambda) = \rho \cdot \frac{2\pi}{k^2} \sum_{n=1}^{\infty} (2n+1) \left(|a_n|^2 + |b_n|^2 \right) \quad (1)$$

where ρ signifies the phosphor granule denseness. σ_{scat} signifies the scattering cross-section. λ signifies the illumination wavelength. k signifies the wavenumber, equaling to $2\pi/\lambda$. a_n and b_n signify the extension coefficients featuring even and odd symmetry. Said coefficients are determined via Equations (2) and (3) (Trang et al., 2019):

$$a_n(x, m) = \frac{\psi_n'(mx)\psi_n(x) - m\psi_n(mx)\psi_n'(x)}{\psi_n'(mx)\xi_n(x) - m\psi_n(mx)\xi_n'(x)} \quad (2)$$

$$b_n(x, m) = \frac{\psi_n'(mx)\psi_n(x) - m\psi_n(mx)\psi_n'(x)}{\psi_n'(mx)\xi_n(x) - m\psi_n(mx)\xi_n'(x)} \quad (3)$$

where x signifies the magnitude parameter, equaling to $k \cdot r$ with r being the particle size. m signifies the refraction index for the dispersal scattering granules. $\psi_n(x)$ and $\xi_n(x)$ signify the Riccati function. As shown by Figure 5(a), the YAG:Ce^{3+} granules within the phosphor sheet disperse illumination via Mie dispersion and as such, the scattering proficiency relies upon the particle magnitude, refraction index contrariety, as well as wavelength. Regarding standard YAG:Ce^{3+} microscopic granules with diametric magnitude between 1 and 10 μm, based on the Mie hypothesis, the scattering cross-section would be approximately twofold the geometrical cross-section in the case of observable wavelength levels (Fujita et al., 2010), indicating that the scattering coefficient is linked to the particle number denseness as shown by Figure 6 and reversely proportional to the particle size, while showing faint sensitivity towards observable wavelengths. The blue photonic granules under small wavelengths see seemingly more potent scattering compared to YAG's yellow discharge due to the size parameter $\frac{2\pi r}{\lambda}$ as well as greater absorptivity under blue zone. For YAG:Ce^{3+}, the absorptivity would be particularly potent under blue zone but insignificant under yellow zone (Loan et al., 2022). As such, the blue InGaN illumination would be practically subject to various dispersion/absorptivity activities within the phosphor, whilst the yellow discharge primarily disperses under limited re-absorptivity. Tiny phosphor granules under significant dosage generate high scattering coefficient, leaning towards isotropy scattering. With the particle magnitude surging, the scattering coefficient swiftly declines while the dispersion leans towards fore-apex under an increasing anisotropic element (Lee et al., 2024). Essentially, extremely tiny granules disperse in an almost homogenous fashion, while huge granules generate noticeable fore lobes. Subsequently, the reduced scattering may become far tinier in the case of big granules, letting illumination traverse further prior to the randomizing process. Said compromise was perceived in an earlier work, showing that the scattering coefficient as well as anisotropic factor display inverse variance under the particle size (Le et al., 2025). Since the refraction index of YAG:Ce^{3+} proves to be greater the silicone latticework, scattering manifests upon every interfacial plane between phosphor and silicone. The Mie hypothesis approximates that in the case of big granules, scattering would be nearly geometrical across observable wavelength levels (Fujita et al., 2010). As such, the scattering coefficient would be primarily influence by geometrical setting instead of relying heavily upon wavelength. In reality, simulation based on Rayleigh or Mie Equations merely exhibit a limited surge for the scattering coefficient under smaller wavelength levels. Alongside the potent blue absorptivity, said mechanism indicates scattering penalty since the InGaN illumination under roughly 450 nm would be far greater compared to the yellow illumination under greater wavelength. Certain works observe that YAG:Ce^{3+} potently absorbs the blue element then casts back in the yellow element, generating a greater blue scattering coefficient compared to the yellow counterpart (Le et al., 2026). Notably, tiny granules yield an almost isotropy scattering, whereas big counterparts

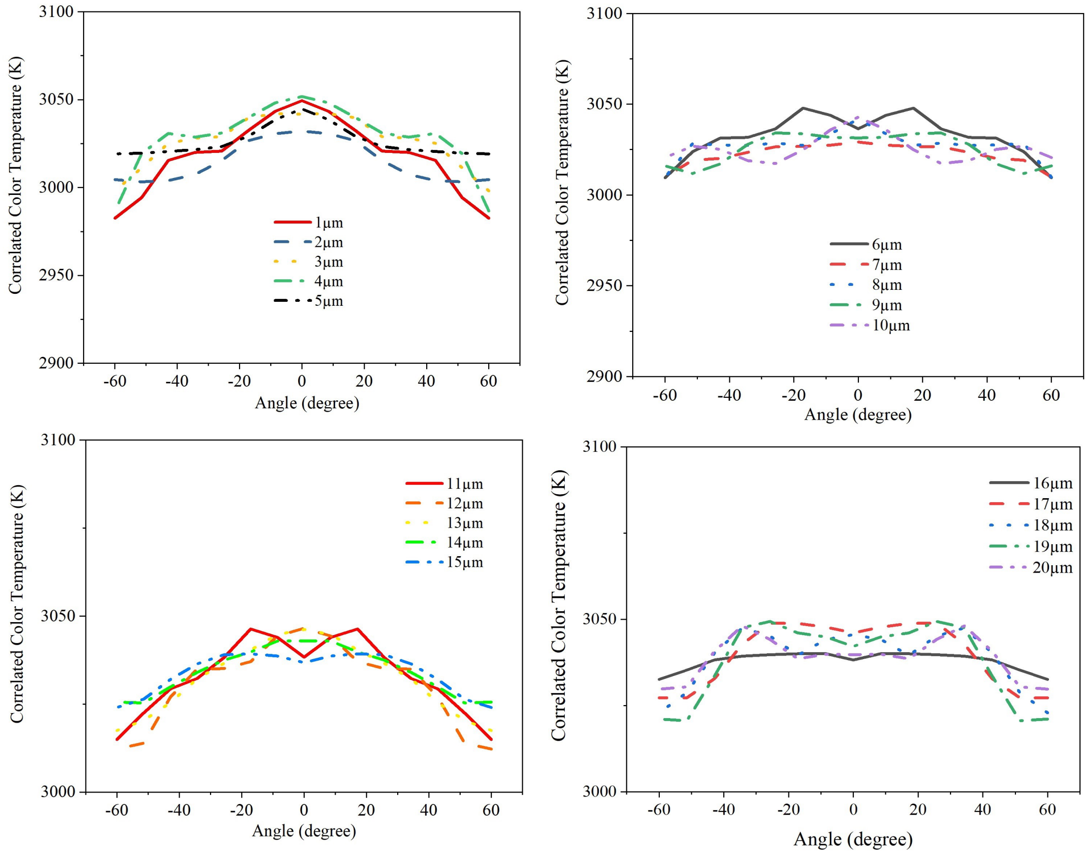

Figure 7. CCT Values with Various Particle Sizes

lead the anisotropic factor towards fore scattering (Loan et al., 2022). If granules are tiny compared to wavelength, every secondary dispersed ripple contributes to phase and barely yields any potent pathway. With the magnitude surging, intrusion generates lobe patterns within the scattering profile, boosting the anisotropic factor. As such, the angle allocation for the dispersed illumination relies upon size as well as wavelength. The small wavelength of InGaN for medium-magnitude YAG granules have a higher chance of scattering more widely compared to the phosphor discharge that gets out of the granule nearly homogenously.

Within the phosphor sheet, repetitive dispersion will randomize photonic pathways. The Lambertian pump illumination generated via the LED chip would be transmuted into a dispersal illumination field. Notably, the Ce^{3+} discharge would be isotropic. According to an earlier study, the transmuted yellow illumination features an isotropy discharge profile, meaning that posterior to absorptivity as well as re-discharge, yellow photonic granules exit the phosphor within every pathway (Ma and Anh, 2024). As a result, the output of the phosphor-transmuted WLED proves to be highly wide-angle, as shown by Figure 5(b). Unabsorbed blue photonic granules have a high chance of being rear-reflected or dispersed sidewise, whilst the yellow discharge pervades broad hard angles. In reality, the merger between Lambertian pump as well as isotropy re-discharge indicates that the far-field leans towards a semi-Lambertian output. The phosphor assists in flattening the angle intenseness data via randomizing the ray. Regardless, every spectrum movement alongside angle, called angle chroma variance, manifests since blue as well as yellow illumination show disparate scattering. Generally, based on hypothesis and assessment, the blue spectrum of InGaN facilitates potent and wavelength-reliant dispersion within the YAG:Ce^{3+} sheet. The scattering coefficient of the phosphor would be biggest under small-wavelength illumination, whilst its re-discharged yellow illumination is subject to limited absorptivity and solely dispersion. Therefore, photonic granules are subject to a particularly dispersal transference within the sheet. Directional at first, illumination would be eventually almost isotropic posterior to various dispersions (Thong et al., 2022). Said association between spectrum absorptivity as well as angle dispersion, based on Mie hypothesis and validated via simulations, decides the optical dispersion mechanism for the phosphor sheets phosphor-transmuted WLED apparatuses. InGaN has the ability to enhance particle sizes by improving light transmission and wavelength conversion efficiency. Blue light brightness may increase when forward scattering and reabsorption decrease and forward emission blue light dispersion increases. This is accomplished by lowering the yellow phosphorus content while increasing particle size, as shown in Figure 6.

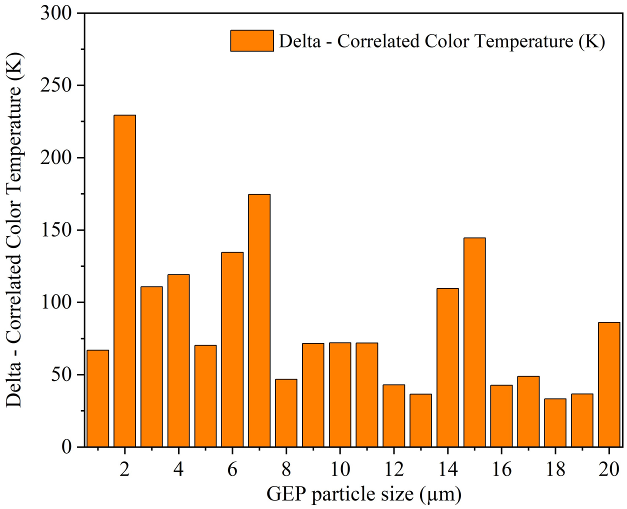

Figure 8. Color Difference Values with Different Particle Sizes

3.3 Influence of InGaN Particles on the Correlated Color Temperature (CCT) and Deviated CCT (D-CCT) of Phosphor-Transmuted WLED

As seen in Figures 7 and 8, CCT (Loan et al., 2022) is not concentration dependent. Figure 7 shows how increased doping can reduce a phosphor's CCT variance. CCT values are highest at temperatures about 3050 K and particle sizes of 6 μm. Figure 8 demonstrate that the D-CCT eventually reaches its lowest value with particle sizes of 8 μm, which is nearly 120 K lower than the result with particle sizes of 7 μm, where the D-CCT value is 170 K. InGaN chips are a key element impacting on CCT as well as D-CCT in phosphor-transmuted WLED apparatuses. Said impact involves spectrum matching as well as scattering discrepancy. The median CCT of the apparatus would be identified via the proportion between propagated blue illumination and transmuted yellow illumination (Trang and Anh, 2025). InGaN chips control said proportion via their spectrum position with the absorptivity band of the phosphor. YAG:Ce^{3+} features its own absorptivity apex, usually focalized at roughly 460 nm. When InGaN chips discharges under said apex, absorptivity would be maximal, generating additional yellow illumination as well as a warmer/smaller CCT (Schweitzer et al., 2014). When the InGaN apex changes because of production binning or functioning states, the absorptivity coefficient declines. Additional blue illumination would not be absorbed when passing through, while a smaller amount of yellow illumination would be induced. Said mechanism generates a spectrum with a strong blue element, considerably boosting the CCT, i.e. creating chiller illumination. When the conducting current surges, the discharge of InGaN chips may change, blue-shifting caused by band pervading or red-shifting caused by heat. Said change alters the pump wavelength across the incline of the YAG absorptivity arch, varying the proportion between blue and yellow. Said mechanism leads to drifting in CCT throughout the functioning process, causing a lack of stability for high-powered WLED apparatuses. In the case of D-CCT, InGaN chips would be responsible the deviation because of the elementary disparity between the way blue as well as yellow photonic granules is created and traverse. The blue illumination would be generated by the InGaN chip exterior then traverse via the phosphor sheet. Because of the Mie dispersion setting, said illumination possesses a significant anisotropic factor, meaning that it favors fore scattering (Huang et al., 2021). As such, it would be condensed at the focal point of the ray (regular observing angle), generating a strong-CCT blue location. Meanwhile, yellow illumination would be created within phosphor granules. Its discharge would be isotropic, discharging identically toward every pathway. It disperses for several instances and exits via the sideways of the WLED package. The InGaN wavelength (roughly 450 nm) sees a greater scattering coefficient compared to the yellow illumination because of the refraction index dispersal of the encasing latticework. In spite of the greater dispersion, the potent fore pathway of the blue incidental illumination prevails, and as such, it cannot be blended extensively like the isotropic yellow discharge (Markovskyi et al., 2023). Said discrepancy would be innate for the task of employing a directional means, such as InGaN, for pumping a volumetric dispersal means, which is YAG in the case.

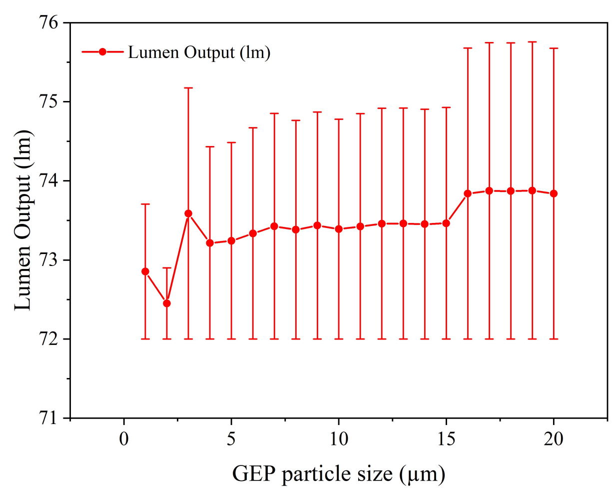

Figure 9. Luminescence Strength with Various Particle Sizes

3.4 Influence of InGaN Particles on the Lumen of Phosphor-Transmuted WLED

Figure 9 indicates that the particle size does not always boost white light emission brightness. Particle sizes of 9 μm produced the best results, whereas particle sizes of 6 μm produced the worst. As a result of increased backscattering and reabsorption, there is less blue emission and an uneven distribution of hues. Larger particle sizes, for example, may cause the phos-

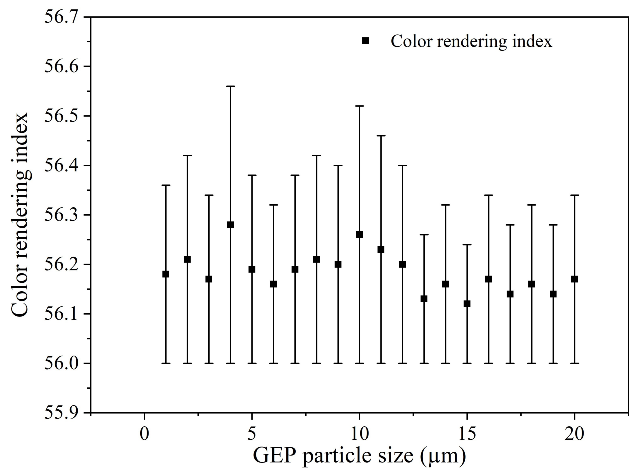

Figure 10. CRI Values with Various Particle Sizes

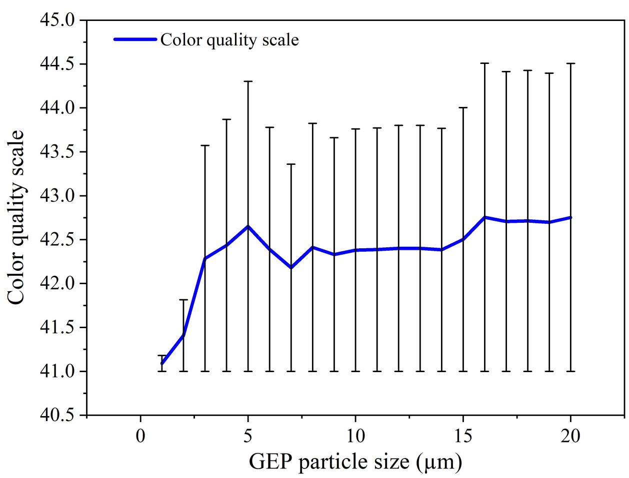

Figure 11. CQS Values with Various Particle Sizes

phor to shift from blue to yellow or orange-red when subjected to more backscattered blue light (Le et al., 2024). Before the phosphor coating may begin to expand, a particular particle size is required. The emission spectrum would be limited due to the multiple reflections that the modified light would acquire from various objects. To put it another way, a high phosphor dose may increase the proportion of back-reflected converted light, boosting CCT while decreasing luminous intensity. Figure 9 demonstrates how using 9 μm particle sizes boosted brightness and color uniformity in a simulated WLED with a lumen output power of around 73.43 lm. When the In presence surges to alter the wavelength from blue (450 nm) to green, the crystalline performance would deteriorate while the piezoelectrical field surges, considerably lessening the EQP (Van Dung and Anh, 2025). Under strong conducting currents needed to accommodate strong-lumen uses, the EQP of the InGaN would decline, or droop, because of Auger recombination as well as conveyor seepage, thus imposing a limit on the maximal lumen produceable by the setting, under any level of proficiency of the YAG phosphor (Cong and Anh, 2025). The power disparity among the pumping InGaN photonic granules and YAG discharged photonic granule leads to an elementary thermodynamical penalty. Blue photonic granules possess greater power compared to the yellow counterparts. As YAG absorbs a blue photonic granule then re-discharges a yellow counterpart, the power disparity would dissipate in the form of heat. The deepness of the blue pump determines the extent for said penalty. Larger power gap leads to greater Stokes penalty and hence additional heat and smaller lumen, while tinier power gap leads to smaller Stokes penalty and hence greater hypothetical proficiency, which is closer to the yellow discharge power (Wang et al., 2024). The blue illumination seeping via the phosphor, for blending and generating white illumination, has a lack of effect on the lumen since human sight would not be responsive towards the blue color at 450 nm. Changing the InGaN discharge towards greater wavelength levels between 460 and 470 nm would shift it closer to the highest responsiveness of human sight, hypothetically boosting the lumen effect on the blue element (Tavazzi et al., 2020). Regardless, it is necessary to balance the InGaN discharge against the YAG absorptivity proficiency. The lumen output relies upon the proficiency in which the discharge spectrum of InGaN chip intersects with the YAG:Ce^{3+} absorptivity exciting band. Since YAG:Ce^{3+} possesses an apex excitation of roughly 460 nm, the InGaN chip discharging under 440 or 480 nm would make contact with the pronounced part of the YAG absorptivity arch. A smaller amount of blue illumination would be transmuted into yellow counterpart that holds the bulk of lumen, resulting in a setting which yields excessive blue illumination (small lumen) while leading to a lack of yellow (high lumen), causing a small luminous flux in general (Sousa et al., 2015). For maximizing lumen, the InGaN chip need to discharge at roughly 460 nm. Said wavelength limits Stokes shift thermic penalties, yields maximal YAG:Ce^{3+} absorptivity to induce yellow illumination with highest lumen and yields greater sight sensitiveness compared to smaller blue wavelength levels.

3.5 Influence of InGaN Particles on the Color Rendition of Phosphor-Transmuted WLED

Figures 10 and 11 illustrate that particle sizes have a significant impact on the brightness and hue rendition of white LEDs (Anh et al., 2025b). The discharge properties of the InGaN chip inherently restricts attainable color rendering indicator (CRI) as well as color quality scale (CQS). Within a conventional blue-pumped YAG:Ce^{3+} setting, said chip usually induces a spectrum deficiency (cyan opening) as well as a spectrum surplus (blue bump), which degrade color performance (Cong and Anh, 2025). The CRI degrades spectrum deviation via a referential blackbody radiator. The InGaN chip affects said element via two primary ways, including the cyan opening and blue bump. Firstly, conventional InGaN chip units discharge a thin band under 450 nm while YAG:Ce^{3+} discharge would peak under 550 nm, leaving a considerable spectrum opening

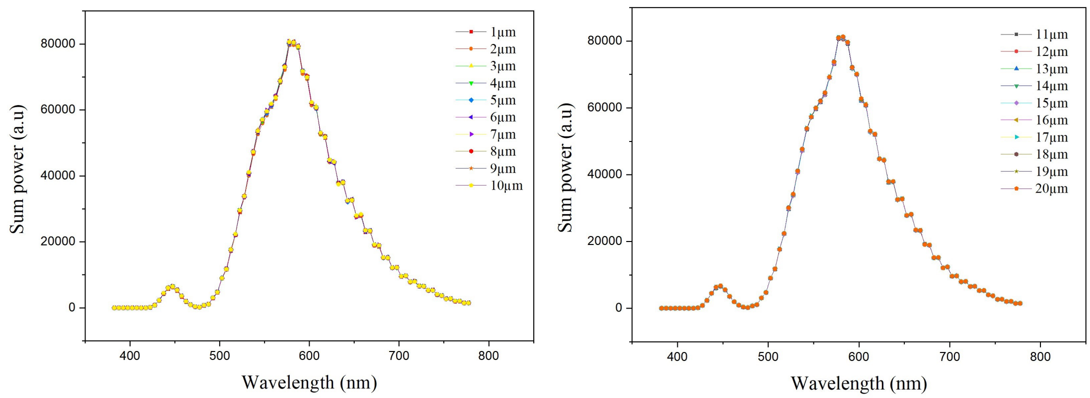

Figure 12. Luminescent Power of the WLED

within the cyan zone between 480 and 500 nm (Jargus et al., 2019). Said opening leads to undesirable chroma rendition relying upon cyan reflectance. When the InGaN apex is moved towards bigger wavelength levels between 460 and 470 nm for eliminating said opening, the YAG transmutation proficiency usually declines while the CRI can be enhanced since the spectrum shows continuity. Secondly, the blue bump and red shortage can also affect CRI (Chen and Huang, 2024). For attaining a particular CCT, a potent, thin InGaN apex would be needed for balancing the wide YAG discharge, creating a bumpy spectrum dissimilar to the even arch of a halogen light. Conventional InGaN-YAG settings would be known for their undesirable deficiency of vivid red under at least 650 nm. Although the InGaN chips is not a discharger of red illumination, their significant blue power would be typically very far away from the red zone for proficiently pumping red-discharging phosphor samples when introduced for balancing the spectrum while avoiding ancillary red elements. Said mechanism usually yields a small CRI as well as an extremely small or negative R9 outcome (saturated red) (Anh et al., 2025a). For circumventing CRI downsides, CQS was proposed, especially in the case of saturated chromas, and is subject to a greater influence from InGaN. Dissimilar to CRI's aversion to all divergences, CQS is more tolerant of boosted chroma saturation. In reality, the potent blue discharge generated via the InGaN chip is able to augment the observed saturation for blue as well as entities with chill chromas. Although CRI may deem said aspect imprecise and yield a small score, CQS can sustain a greater score since it considers the taste regarding saturated chromas (Pintus et al., 2021). Similar to CRI, CQS proves responsive towards the spectral continuousness. A significant cyan opening resulting from a thin 450-nm InGaN apex would still degrade the CQS outcome since it signifies a lacking part for the observable spectrum needed to precisely manifest intricate chroma blends. Color rendition investigations using the CRI and CQS revealed that as particle sizes increased to 10 μm, their values fluctuated significantly. The unpredictability of green, yellow-orange, as well as blue hues could become connected with CRI and CQS declines. High particle sizes provide irregular light emission with a preference for the yellow-orange spectrum, as well as improved dispersion. The InGaN chips yield a spectrum limit upon chroma performance. Their thin, small-wavelength discharge generates the distinctive cyan opening which restricts conventional YAG:Ce^{3+} WLED apparatuses to lower CRIs. Adjusting the InGaN discharge for bigger wavelength levels that approach the range between 460 and 470 nm would be a straightforward technique for augmenting CRI as well as CQS via closing the spectrum opening among the pumping means and the phosphor discharge. As we evaluate the findings, we will adjust the CRI and CQS of this phosphor, as well as investigate other parameters such as particle size (Tung et al., 2024).

3.6 Influence of InGaN Particles on the Spectrum Power of Phosphor-Transmuted WLED

The correlation between spectral power and various ranges of InGaN particle sizes is illustrated in Figure 12, displaying particle sizes from 1 to 10 μm and from 11 to 20 μm. Particle sizes have been discovered to boost the blue and orange-red parts of the white light spectrum. To improve lighting efficiency, light scattering and absorption patterns in particle sizes can be altered. The greatest peaks are within blue (450 nm) along with yellow-orange (about 600 nm) wavelength ranges. With a particle size range of 1 to 10 μm, the spectral power exhibits two distinct peaks within the wavelength range of 400 to 800 nm. During its initial apex, the spectral power reaches its minimum, exhibiting no variation within the wavelength range of 400 to 420 nm. However, as the wavelength approaches approximately 450 nm, the spectral power exhibits a notable and sustained increase across most particle sizes within this range, prior to attaining its peak at approximately 450 nm. As the wavelength exceeds 450 nm, the spectral power exhibits a correspondingly notable decrease reaching 480 nm, which is nearly as low as its value at 420 nm. During the second peak, the spectral power exhibits a consistent pattern of variation across all particle sizes, beginning at a low level, then rising sharply to reach its maximum at approximately 590 nm median wavelength, and subsequently declining thereafter. The spectral power within a particle size range of 11 to 20 wt.% over the same wavelength range also exhibits dual peaks. Compared to the particle size range of 1 to 10 wt.%, the spectral power within the 11 to 20 wt.% range exhibits more pronounced fluctuations and less consistent surges, although its overall pattern of variation remains partially similar. The InGaN chip can determine the form, balance as well as consistency of the spectrum power distribution (SPD) (Ma and Anh, 2024). The SPD in YAG:Ce^{3+} WLEDs would be a merger between two disparate discharges, including the thin blue discharge generated via the InGaN chip, called propagated illumination, as well as the wide yellow discharge generated by YAG, called transmuted illumination. Said chip affects these elements via several primary phenomena, including the cyan opening and blue bump stated above along with the yellow energy called exciting proficiency. The chip would non-directly regulates the intenseness for the wide yellow element between 500 and 700 nm via the proficiency in which it would pump the phosphor (Nguyen et al., 2023). As mentioned above, the illumination-absorbing ability of YAG:Ce^{3+} would be highest at roughly 460 nm. When the chip discharges under 460 nm, spectrum energy transference would be maximal. When the chip discharges under 440 nm, it would make contact with the pronounced part of the YAG absorptivity arch. The majority of blue illumination bypasses while avoiding transmutation, leading to a contorted SPD featuring excessive blue energy as well as deficient yellow energy (Du et al., 2021). Under strong current, InGaN exhibits efficiency droop, abating its quantum proficiency and the entire height of SPD. The power disparity among the absorbed InGaN photonic granules and the discharged YAG counterpart would dissipate in the form of heat, indicating Stokes shift (Wang et al., 2010). An InGaN chip with a smaller wavelength and hence greater power will boost said thermic penalty, abating the radioactive energy applying to the yellow portion in the spectrum. InGaN chips function in the form of adjuster of the spectrum energy in WLED, straightforwardly yielding the huge-power blue element whilst regulating the intenseness for yellow element via its spectrum position with the absorptivity band of the phosphor (Zhao et al., 2023). Comparison has been made between InGaN and its counterparts from previous studies to highlight its applicability to optical apparatuses, which is shown by Tables 1 and 2. InGaN yield comparable optical attributes compared to its counterparts SiO_2 and KBr. However, it offers a much smaller scattering, thus making it suitable for high-power directional LEDs, display LEDs and micro-LEDs.

4. CONCLUSIONS

In brief, blue, green, and yellow LEDs were effectively realized using organized NCs with lengthy InGaN activating areas. The lengthy InGaN sections proved to be free of flaws with just twin limits identified at the higher GaN:Mg area, probably owing to the minimal heat utilized for development. Pulsed EL measurements possibly reaching 1900 A cm^{-2} revealed no sink or saturation for the effectiveness, whereas the emitting wavelength shows just one minor blue change, which is practically insignificant for the yellow gadget (568 nm). Furthermore, the emitting line widths were found to be decreasing. Finally, the determined line width ratios are somewhat greater than those published for planar MQW layouts but are comparable to or superior to those published for organized nano-LEDs utilizing InGaN QDisks. Because they mix the positive aspects of directed NCs (strong uniformity quality, illumination extraction effectiveness, etc.) with the advantages of a thick InGaN activating area (a decrease of Auger re-mixture and current over flow process) without crystal quality deterioration, the nano-LEDs with built thick InGaN areas can be of interest in illumination uses. InGaN was also utilized in a phosphor-transmuted white LED (WLED) to enhance its optical attributes such as scattering, lumen, and color rendition. It was found that InGaN has its own advantages and limitations. It was found that adjusting the InGaN discharge to 460 nm would benefit the lumen and color rendition of the WLED under a particle size of 9 μm, while a 450-nm discharge would promote scattering, both of which better match the human sight.

5. ACKNOWLEDGEMENT

This research is supported by Industrial University of Ho Chi Minh City (IUH) under grant number 78/HD-DHCN, dated day 22 month 12 year 2025.

REFERENCES

Aktas, M., S. Grzanka, Ł. Marona, J. Goss, G. Staszczak, A. Kafar, and P. Perlin (2024). Polarization-Doped InGaN LEDs and Laser Diodes for Broad Temperature Range Operation. *Materials*, **17**(18); 4502

Albert, S., A. Bengoechea-Encabo, M. Sanchez-Garcia, E. Calleja, and U. Jahn (2013). Selective Area Growth and Characterization of InGaN Nanocolumns for Phosphor-Free White Light Emission. *Journal of Applied Physics*, **113**(11); 114306

An, Y., K. Ren, L. Yin, and J. Zhang (2023). Modeling on Monolithic Integration Structure of AlGaN/InGaN/GaN High Electron Mobility Transistors and LEDs: 2DEG Density and Radiative Recombination. *Electronics*, **12**(5); 1087

Anh, N. D. Q., S. D. Ho, P. T. M. Man, T. K. Duy, and N. T. P. Loan (2025a). Obtaining Higher LED Lighting Chromaticity and Luminosity with SiO_2 Particles at Different Diameters. *Journal of Advanced Engineering and Computation*, **9**(1); 21

Anh, N. D. Q., N. T. P. Loan, P. V. De, and H. Y. Lee (2025b). KBr Scattering Simulation for Improving Phosphor-Converting White LED Performance. *Optoelectronics and Advanced Materials - Rapid Communications*, **19**(7–8); 378–383

Baheti, P. D., R. A. Talewar, and S. Moharil (2023). Blue

LED (InGaN)-Driven Yellow and Red Emitting Phosphor for White Light Generation. *Materials Letters*, **348**; 134727

Barettin, D., A. V. Sakharov, A. F. Tsatsulnikov, A. E. Nikolaev, A. Pecchia, M. A. D. Maur, and N. Cherkashin (2023). Impact of Local Composition on the Emission Spectra of InGaN Quantum-Dot LEDs. *Nanomaterials*, **13**(8); 1367

Bercha, A., M. Chlipała, M. Hajdel, G. Muzioł, M. Siekacz, H. Turski, and W. Trzeciakowski (2025). Photoluminescence and Photocurrent from InGaN/GaN Diodes with Quantum Wells of Different Widths and Polarities. *Nanomaterials*, **15**(2); 112

Cakmakci, O., Y. Qin, P. Bosel, and G. Wetzstein (2021). Holographic Pancake Optics for Thin and Lightweight Optical See-Through Augmented Reality. *Optics Express*, **29**(22); 35206

Chen, X. and X. Huang (2024). Full-Visible-Spectrum White LEDs Enabled by a Blue-Light-Excitable Cyan Phosphor. *ACS Applied Materials & Interfaces*, **16**(42); 57365–57376

Cong, P. H. and N. D. Q. Anh (2025). Augmenting Chroma Performance for WLED Employing $Sr8ZnSc(PO_4)_7$:Eu^{2+}@SiO_2 as a Scattering-Enhancing Substance. *Science & Technology Indonesia*, **10**(2); 467–472

Cong, P. H., N. T. P. Loan, N. D. Q. Anh, and H. Lee (2025). Influence of Potassium Bromide Phosphor on Optical Properties of White Light-Emitting Diodes. *International Journal of Advances in Applied Sciences*, **14**(4); 1359

Du, A., Q. Du, X. Liu, Y. Yang, C. Xia, J. Zou, and J. Li (2021). Ce: YAG Transparent Ceramics Enabling High Luminous Efficacy for High-Power LEDs/LDs. *Journal of Inorganic Materials*, **8**(36); 884–892

Duan, Y., N. Zhao, C. Chen, H. Lin, S. Lin, Y. Li, and H. Chen (2025). Photo-Thermal Crosstalk in AlGaInP and InGaN LEDs under Dual-Wavelength Excitation. *Available at SSRN 5954466*

Enya, Y., Y. Yoshizumi, T. Kyono, K. Akita, M. Ueno, M. Adachi, T. Sumitomo, S. Tokuyama, T. Ikegami, K. Katayama, et al. (2009). 531 nm Green Lasing of InGaN Based Laser Diodes on Semi-Polar {2021} Free-Standing GaN Substrates. *Applied Physics Express*, **2**(8); 082101

Fujita, S., Y. Umayahara, and S. Tanabe (2010). Influence of Light Scattering on Luminous Efficacy in *Ce:YAG* Glass-Ceramic Phosphor. *Journal of the Ceramic Society of Japan*, **118**(1374); 128–131

Grzanka, E., S. Bauer, A. Lachowski, S. Grzanka, R. Czernecki, B. So, and M. Leszczyński (2025). In Situ X-Ray Study During Thermal Cycle Treatment Combined with Complementary Ex Situ Investigation of *InGaN* Quantum Wells. *Nanomaterials*, **15**(2); 140

Gu, Y., Y. Gong, P. Zhang, H. Hua, S. Jin, W. Yang, J. Zhu, and S. Lu (2023). Investigation on the Optical Properties of Micro-LEDs Based on InGaN Quantum Dots Grown by Molecular Beam Epitaxy. *Nanomaterials*, **13**(8); 1346

Hadi, D. S., H. Wafda, A. P. A. Mustari, V. Trisnawan, N. Widiawati, F. Miftasani, and D. H. Prajitno (2025). Corrosion Behavior of Modified F/M Steel with Ti and Dispersed Oxides: Y_2O_3 and ZrO_2 Under High Temperature in Static Liquid Lead. *Science & Technology Indonesia*, **10**(3); 877–888

Han, Q., W. Cai, J. Wang, Y. Furusawa, H. Wang, X. Li, H. Cheong, Y. Honda, and H. Amano (2026). Red-Emitting μ LEDs Based on Graded-Indium InGaN Nanoplatelets. *Japanese Journal of Applied Physics*, **65**(2); 026501

Hou, Y., X. Su, W. Chen, and W. Zhao (2021). Calibration Method of Multi-Projector Display System with Extra-Large FOV and Quantitative Registration Accuracy Analysis. *Optics Express*, **29**(22); 36704

Hsieh, T., W. Huang, K. Hong, T. Lee, Y. Bai, Y. Pai, and H. Kuo (2023). Optoelectronic Simulations of InGaN-Based Green Micro-Resonant Cavity Light-Emitting Diodes with Staggered Multiple Quantum Wells. *Crystals*, **13**(4); 572

Huang, J., Y. Ni, Y. Ma, Y. Li, Z. Sun, X. Zhu, and H. Chen (2021). Composite Structure Cr:YAG/Ce:YAG and (Ce,Cr):YAG/Ce:YAG Transparent Ceramics with High Color Rendering Index for White LEDs/LDs. *Ceramics International*, **47**(8); 11415–11422

Huang, W., X. Miao, and Z. Liu (2023). Investigations of Sidewall Passivation Using the Sol-Gel Method on the Optoelectronic Performance for Blue InGaN Micro-LEDs. *Micromachines*, **14**(3); 566

Jafar, N., J. Jiang, H. Lu, M. Qasim, and H. Zhang (2023). Recent Research on Indium-Gallium-Nitride-Based Light-Emitting Diodes: Growth Conditions and External Quantum Efficiency. *Crystals*, **13**(12); 1623

Jargus, J., J. Vitasek, J. Nedoma, V. Vasinek, and R. Martinek (2019). Effect of Selected Luminescent Layers on CCT, CRI, and Response Times. *Materials*, **12**(13); 2095

Kishino, K., K. Nagashima, and K. Yamano (2013). Monolithic Integration of InGaN-Based Nanocolumn Light-Emitting Diodes with Different Emission Colors. *Applied Physics Express*, **6**(1); 012101

Kong, X., S. Albert, A. Bengoechea-Encabo, M. A. Sanchez-Garcia, E. Calleja, and A. Trampert (2012). Plasmon Excitation in Electron Energy-Loss Spectroscopy for Determination of Indium Concentration in (In,Ga)N/GaN Nanowires. *Nanotechnology*, **23**(48); 485701

Le, P. X., N. D. Q. Anh, and H. Y. Lee (2024). Regulating the White LED Properties with Different SiO_2 Particle Sizes. *Optoelectronics and Advanced Materials – Rapid Communications*, **18**(9–10); 485–489

Le, P. X., N. T. P. Loan, and N. D. Q. Anh (2026). Optical Assessment of Titanium Oxide Employed in Phosphor-Transmuted WLED Devices. *Science & Technology Indonesia*, **11**(1); 345–355

Le, P. X., N. T. P. Loan, N. D. Q. Anh, and H. Lee (2025). Thermally Stable Sol-Gel $Y_3Al_5O_{12}$:Ce^{3+} Phosphors for White Light-Emitting Diodes. *International Journal of Advances in Applied Sciences*, **14**(4); 1367–1374

Lee, T., C. Huang, W. Miao, F. Hsiao, C. Tsai, Y. Hung, and H. Kuo (2024). Innovative Stacked Yellow and Blue Mini-LED Chip for White Lamp Applications. *Micromachines*,

15(6); 796

Loan, N. T. P., N. D. Q. Anh, N. C. Trang, and H. Lee (2022). Better Color Distribution Uniformity and Higher Luminous Intensity for LED by Using a Three-Layered Remote Phosphor Structure. *Materials Science-Poland*, **40**(1); 60–67

Ma, H. and N. D. Q. Anh (2024). Review the Influence of Aluminum-ZnO Films on Multi-Chip Remote-Phosphor White LEDs' Properties. *Journal of Advanced Engineering and Computation*, **8**(4); 225

Markovskyi, A., V. Gorbenko, T. Zorenko, S. Witkiewicz-Lukaszek, O. Sidletskiy, A. Fedorov, and Y. Zorenko (2023). Development of Three-Layered Composite Color Converters for White LEDs Based on the Epitaxial Structures of YAG:Ce, TbAG:Ce and LuAG:Ce Garnets. *Materials*, **16**(5); 1848

Miao, W., Y. Hong, F. Hsiao, J. Chen, H. Chiang, C. Lin, and H. Kuo (2023). Modified Distributed Bragg Reflectors for Color Stability in InGaN Red Micro-LEDs. *Nanomaterials*, **13**(4); 661

Nguyen, Q., B. Glorieux, G. Sebe, T. Yang, Y. Yu, and C. Sun (2023). Passive Anti-Leakage of Blue Light for Phosphor-Converted White LEDs with Crystal Nanocellulose Materials. *Scientific Reports*, **13**(1); 13039

Oh, S., J. Lee, and J. Lim (2025). A Control Method for Optimizing the Spectral Ratio Characteristics of LED Lighting to Provide Color Rendering Performance Comparable to Natural Light. *Sensors*, **25**(24); 7453

Pintus, V., F. Szabó, R. Gazdag-Kéri, D. N. Tóth, R. Nagy, P. Csuti, and M. Schreiner (2021). The Effect of New LED Lighting Systems on the Colour of Modern Paints. *Scientific Reports*, **11**(1); 22375

Qin, H., S. Zhang, Q. Fan, X. Ni, L. Tao, and X. Gu (2025). Dielectric Passivation Treatment of InGaN Mesa on Si Substrates for Red Micro-LED Application. *Crystals*, **15**(3); 267

Qiu, L., H. Ye, G. Xiong, W. Zhang, Y. Huang, Q. Liang, and Z. Feng (2025). Sm^{3+}-Activated $KLa(WO_4)_2$ Phosphors with Gd^{3+} Co-Doping: Orange-Red Emission and Thermal Stability toward Potential Plant Lighting Applications. *Journal of Solid State Chemistry*, **355**; 125784

Rianjanu, A., T. Haloho, J. L. Pasaribu, A. G. Fahmi, E. Nurfani, W. S. Sipahutar, H. T. Yudistira, and T. Taher (2025). Electrospun Rare-Earth Metal Oxide (CeO_2) Nanofiber for the Degradation of Congo Red Aqueous Dyes. *Science & Technology Indonesia*, **10**(1); 123–130

Schweitzer, S., C. Sommer, P. Hartmann, P. Fulmek, J. Nicolics, P. Pachler, H. Hoschopf, F. Schrank, G. Langer, and F. P. Wenzl (2014). A Comprehensive Discussion on Colour Conversion Element Design of Phosphor Converted LEDs. *Journal of Solid State Lighting*, **1**(1); 18

Sousa, M. A., T. C. Esteves, N. B. Sedrine, J. Rodrigues, M. B. Lourenço, A. Redondo-Cubero, and T. Monteiro (2015). Luminescence Studies on Green Emitting InGaN/-GaN MQWs Implanted with Nitrogen. *Scientific Reports*, **5**(1); 9703

Sun, H., Y. Chen, Y. Ben, H. Zhang, Y. Zhao, Z. Jin, and M. Zhou (2023). Influence of Low-Temperature Cap Layer Thickness on Luminescence Characteristics of Green InGaN/GaN Quantum Wells. *Materials*, **16**(4); 1558

Tavazzi, S., F. Cozza, G. Nigrotti, C. Braga, N. Vlasak, S. Larcher, and F. Zeri (2020). Improvement or Worsening of Human Contrast Sensitivity due to Blue Light Attenuation at 450 nm. *Clinical Optometry*, **12**; 57–66

Thong, N. D. M., D. N. H. Son, S. D. Ho, N. D. Q. Anh, and H. Lee (2022). The Use of $Y_3Al_5O_{12}$:Ce^{3+} and $CaTiO_3$:Pr^{3+} in a Dual-Layer Remote Phosphor Configuration Improves the Optical Efficiencies of a Phosphor-in-Glass White Light-Emitting Diode. *Journal of Advanced Engineering and Computation*, **6**(1); 36

Tourbot, G., C. Bougerol, A. Grenier, M. D. Hertog, D. Sam-Giao, D. Cooper, and B. Daudin (2011). Structural and Optical Properties of InGaN/GaN Nanowire Heterostructures Grown by PA-MBE. *Nanotechnology*, **22**(7); 075601

Trang, L. T. and N. D. Q. Anh (2025). Influences from SiO_2 Particles on Optical Properties of White Diodes Verified Through Computer Simulation. *Indonesian Journal of Electrical Engineering and Computer Science*, **38**(3); 1572–1579

Trang, T. T., N. H. K. Nhan, M. Tran, and P. T. Tin (2019). Yellow-Emitting YAG:Ce Phosphor: Influence of Particle Size on Optical Efficiency of High Color Temperature Conformal Packaging WLEDs. *Digest Journal of Nanomaterials and Biostructures*, **14**(1); 167–173

Tung, H. T., M. H. N. Thi, and N. D. Q. Anh (2024). Improved Color Uniformity in White Light-Emitting Diodes Using $LiLu(MoO_4)_2$:Sm^{3+} Combined SiO_2 Composite. *International Journal of Technology*, **15**(1); 8

Van Dung, N. and N. D. Q. Anh (2025). $Ba_3GdNa(PO_4)_3F$:Eu^{2+} Phosphor with Blue-Red Emission Colors on White-LED Properties. *Indonesian Journal of Electrical Engineering and Computer Science*, **38**(3); 1564–1571

Wang, F., H. Pan, W. Mao, and D. Wang (2024). Optimizations of Luminescent Materials for White Light Emitting Diodes toward Healthy Lighting. *Heliyon*, **10**(14); e34795

Wang, J., L. Wang, W. Zhao, Z. Hao, and Y. Luo (2010). Understanding Efficiency Droop Effect in InGaN/GaN Multiple-Quantum-Well Blue Light-Emitting Diodes with Different Degree of Carrier Localization. *Applied Physics Letters*, **97**(20); 201112

Wang, M., S. Wang, R. Chen, M. Zhu, Y. Liu, H. Ding, and H. Li (2023). Highly Efficient and Stable $CsPbBr_3$-Alginic Acid Composites for White Light-Emitting Diodes. *Coatings*, **13**(6); 1062

Wang, Y., W. Kuang, M. Shang, and Z. Huang (2021). Two-Color Super-Resolution Localization Microscopy via Joint Encoding of Emitter Location and Color. *Optics Express*, **29**(21); 34797

Xiong, Q., H. Liu, Z. Chen, Y. Tai, J. Shi, and W. Liu (2021). Detection of Binocular Chromatic Fusion Limit for Opposite Colors. *Optics Express*, **29**(22); 35022

Xu, F., X. Meng, Y. Xue, Z. Xie, G. Yu, and B. Zhang (2025). Wafer-Scale Hybrid Integration of Micro-LED Arrays with Ultra-Small Pixels on Si Platform. *Journal of Luminescence*, **292**; 121717

Yan, J., Y. Xiang, L. Zhong, C. Jiang, and M. Wu (2025). Broadband Near-Infrared Phosphor $Na_2Mg_5Si_{12}O_{30}:Cr^{3+}$ for Versatile Applications. *Journal of Alloys and Compounds*, **1050**; 185677

Yang, H., Y. Li, J. Wang, A. Li, K. Li, C. Xu, and F. Yun (2023). Power-Dependent Optical Characterization of the InGaN/GaN-Based Micro-Light-Emitting-Diode (LED) in High Spatial Resolution. *Nanomaterials*, **13**(13); 2014

Zhao, M., H. Liao, M. S. Molokeev, Y. Zhou, Q. Zhang, Q. Liu, and Z. Xia (2019). Emerging Ultra-Narrow-Band Cyan-Emitting Phosphor for White LEDs with Enhanced Color Rendition. *Light: Science & Applications*, **8**(1); 38

Zhao, X., K. Sun, S. Cui, B. Tang, H. Hu, and S. Zhou (2023). Recent Progress in Long-Wavelength InGaN Light-Emitting Diodes from the Perspective of Epitaxial Structure. *Advanced photonics research*, **4**(9); 2300061

Zheng, X., G. Zhao, Y. Dai, Y. Fu, M. Zhou, T. Huang, and W. Guo (2025). V-Pit-Induced Electric Field Redistribution Enabling Efficient Hole Injection in InGaN-Based Red Light-Emitting Diodes Grown on Silicon. *PhotoniX*, **6**(1); 55

Zhou, X., J. Zhou, L. Xiao, Z. Tang, C. Cai, T. Zhong, and R. Zhang (2025). Zero-Dimensional Organic-Inorganic Metal Chloride $(C_9H_{13}N_2)_2MnCl_4$ with Highly Efficient Yellow Emission for White Light-Emitting Diode and Flexible X-Ray Imaging. *Journal of Luminescence*, **291**; 121718

